X-ray Crystallographic and Hydrogen Deuterium Exchange Studies Confirm Alternate Kinetic Models for Homolog Insulin Monomers

Esra Ayan[1], Miray Türk[2], Özge Tatlı[3,4], Elek Telek[5], Baran Dingiloğlu[2], Gizem Dinler-Doğanay[2] and Hasan DeMirci[1,6*]

[1] Department of Molecular Biology and Genetics, Faculty of Science, Koç University, Istanbul 34450, Türkiye
[2] Department of Molecular Biology-Genetics and Biotechnology, Istanbul Technical University, Istanbul 34469, Türkiye
[3] Division of Translational Cancer Research, Department of Laboratory Medicine, Lund University, Lund, Sweden
[4] Department of Molecular Biology and Genetics, Istanbul Medeniyet University, 34720, Istanbul, Türkiye
[5] Department of Biophysics, Medical School, University of Pécs, Szigeti Str. 12, H-7624 Pécs, Hungary
[6] Stanford PULSE Institute, SLAC National Laboratory, 94025, Menlo Park, CA, USA

* To whom correspondence should be addressed. Tel: +905525226354; Email: hdemirci@ku.edu.tr & hdemirci@stanford.edu

Abstract

Despite the crucial role of various insulin analogs in achieving satisfactory glycemic control, a comprehensive understanding of their dynamic mechanisms still holds the potential to further optimize ultra-fast-acting insulin analogs, thus significantly improving the well-being of individuals with Type 1 Diabetes. Here, we present new insights derived from our 2.5 Å resolution X-ray crystal structure of modified insulin analog at ambient temperature. Furthermore, we obtained a distinctive side-chain conformation of the Asn3 residue on the B chain (AsnB3) by operating a comparative analysis with a previously available cryogenic rapid-acting insulin structure (PDB_ID: 4GBN). Additionally**,** we employed hydrogen-deuterium exchange mass spectrometry to decipher the molecular dynamics of these insulin analogs. A comparative analysis of H/D dynamics demonstrated that the modified insulin exchanges deuterium atoms faster and more extensively than the intact insulin aspart. The hybrid structural approach combined with computational analysis employed in this study provides novel insight into the structural dynamics of newly modified insulin and insulin aspart monomeric entities. It allows further molecular understanding of intermolecular interrelations driving dissociation kinetics and, therefore, a fast action mechanism.

Introduction

Extensive research has been dedicated to insulin therapy, emphasizing the diverse benefits offered by insulin analogs compared to native human insulin. Subsequent advancements in insulin therapy have led to the approval of rapid-acting insulin analogs designed to replicate

better the bolus secretion of physiological insulin (Home, 2012). The initial formulation in this category, insulin lispro (Humalog^{TM}), received approval in 1996, followed by insulin aspart (IAsp) (NovoLog^{TM}) in 2002 and insulin glulisine (Apidra^{TM}) in 2004 (Heise et al., 2015). More recently, a novel class of insulins known for an even faster action profile, termed "ultra-rapid-acting" insulins, has been introduced, with faster-acting insulin aspart (marketed as Fiasp) receiving approval in 2017 (Hsu et al., 2021). Faster-acting insulin aspart (FIAsp) has an innovative formulation incorporating niacinamide and L-arginine, leading to an accelerated initial absorption compared to insulin aspart (IAsp). Subcutaneous administration of FIAsp has demonstrated superior early glucose-lowering efficiency and efficacy compared to IAsp (Hsu et al., 2021). Regarding mechanism, FIAsp exhibits enhanced compatibility for insulin pump use compared to IAsp and other analogs of rapid-acting insulins (Dutta et al., 2023; Hsu et al., 2021). The latest ultra-rapid-acting insulins introduce additional bolus insulin alternatives for individuals with type 1 or type 2 diabetes (T1D, T2D) (Avgerinos et al., 2021). Key advantages of these ultra-rapid-acting agents include potential improvements in glycemic control for patients with unmet postprandial glucose (PPG) targets, suitability for use in infusion pumps, and their availability in user-friendly pen delivery devices (Stamati et al., 2022). These ultra-rapid-acting insulins offer a rapid onset of action through accelerated insulin absorption and quicker attainment of maximum insulin concentration than traditional short- and rapid-acting insulins (Avgerinos et al., 2021; Stamati et al., 2022). However, an understanding of the kinetics of monomers or oligomers in rapid-acting insulins remains limited. One of the most commonly pursued strategies within this context involves exploring comparative dynamical mechanisms intrinsic to rapid-acting insulins. Attaining a profound understanding of insulin's intricate conformation is acknowledged as the quintessential analytical characterization approach, as it facilitates the discrimination of pivotal regions crucial for mediating insulin-receptor interactions.

This study attempted to elucidate the underlying mechanism governing the dynamic changes in the monomer of less-stable insulin analog compared to its counterpart, IAsp. This was achieved by introducing a mutation in the Arg22 residue on the B chain, replacing it with a more flexible lysine residue together with an already existing substitution at the 28th residue on chain B from proline to aspartic acid, and investigating its impact on protein stability and electrostatic interactions (hereafter referred to as INSv). The model system employed for this study was IAsp

(Simpson and Spencer, 1999). In the initial phase, the surface arginine 22 residue in the B chain of insulin aspart mutated to lysine, considering the protein's foldability. Subsequently, the stability of this variant monomer was assessed using the differential scanning calorimetry technique. Additionally, the intrinsic and distinct dynamics of the monomer were explored through hydrogen-deuterium exchange mass spectrometry (HDX-MS) analysis, and a comparative study was performed with IAsp's monomer. The findings from this experimental approach were further validated computationally by employing Gaussian Network Model (GNM) analysis. Finally, a 2.5 Åresolution X-ray crystal structure was determined through the newly developed multi-well X-ray crystallography technique conducted at ambient temperature, elucidating the conformational dynamics differences between the hexamers of both INSv and IAsp.

Methods

Production of Recombinant LysB22-AspB28 Double Mutant (INSv)

The recombinant INSv gene was cloned to the pET28a(+) vector and was transformed into the *E. coli* BL21 Rosetta-2 strain for overexpression. Bacterial cell cultures, each containing the recombinant INSv protein genes, were cultivated independently in 6 liters of either standard LB-Miller media or Terrific Broth (TB), supplemented with the final concentration of 35 µg/mL chloramphenicol and 50 µg/mL kanamycin at 37°C. Cultures were agitated by using a New Brunswick Innova 4430R shaker at 110 rpm until they reached to an optical density at 600 nm (OD_{600}) of approximately 0.7 for each culture. Recombinant protein expression was induced with Isopropyl b-D-1-thiogalactopyranoside (IPTG) at a final concentration of 0.4 mM. The incubation for protein overexpression was conducted at 37°C for 4 hours. Subsequently, cells were harvested at 4°C using a Beckman Allegra 15R desktop centrifuge at 3500 rpm for 20 minutes. Verification of protein expression was conducted through precast TGX-mini protean gradient SDS-PAGE from BioRad.

The solubilization process of INSv

For the partial purification and complete solubilization of inclusion bodies, cell pellets (1 gram) containing INSv proteins were individually resuspended in 10 mL of lysis buffer containing 25 mM Tris-HCl, pH 8.0, 5 mM Ethylenediaminetetraacetic acid (EDTA) and subsequently homogenized. Bacterial cells were lysed via sonication, and the resulting cell debris underwent low-speed centrifugation (6000 × g, 4°C, 7 minutes). The obtained pellets were subjected to suspension in wash buffer A containing 25 mM Tris-HCl, pH 8.0, 5 mM EDTA supplemented with 0.1% (v/v) Triton X-100 and 1 M urea, followed by wash buffer B containing 25 mM Tris and 2 M urea. The suspension was sonicated for 30 seconds in an ice bath and then centrifuged (8000 × g, 4°C, 20 minutes). To further isolate inclusion bodies, the debris was resuspended at 0.1 g/mL in binding buffer containing 25 mM Tris-HCl, pH 8.4, and 5 mM 2- mercaptoethanol (BME) for INSv, which contained 8 M urea. Centrifugation at 10,000 × g for 30 minutes at 4°C allowed recovery of inclusion bodies containing the fusion proteins, and the resulting supernatants were filtered through a 0.2-micron Millipore filter.

Purification, refolding, and tryptic digestion process of insulin

Sulfitolysis of INSv was conducted at 25°C for 4 hours using 200 mM sodium sulfite (Na_2SO_3) and 20 mM sodium tetrathionate ($Na_2S_4O_6$). Subsequently, the manual gravity Ni-NTA affinity chromatography was employed, involving column equilibration with one column volume of a buffer containing 25 mM Tris-HCl, pH 8.0, 5 mM BME, and 8 M urea and elution with a buffer containing 25 mM Tris-HCl, pH 8.0, 5 mM BME, 8 M urea, and 250 mM imidazole. The protein sample purity was assessed at each stage through 20% SDS-PAGE gel analysis and Coomassie staining. High-purity fractions were collected and filtered through a 0.2-micron Millipore filter. The INSv refolding process is completed by using standard published protocols (Khosravi et al., 2022; Kim et al., 2015; Min et al., 2011). Purified proinsulin (0.5 mg/mL) underwent dialysis against 25 mM Tris-HCl pH 9.00 with 8 M urea and 0.5 mM EDTA at 4°C. After centrifugation (10.000 × g, 4°C, 30 minutes) to remove potential aggregates, the resulting mixture was dialyzed in a refolding solution with 0.1 M Gly/NaOH at pH 10.5, 0.5 M urea, 0.5 mM EDTA, 5% glycerol, and stirred at 15°C overnight. Refolded INSv was further dialyzed against 25 mM Tris-HCl, pH 8.0, with 5% glycerol for 18 hours. Proinsulin underwent tryptic cleavage using trypsin 1:1000 (v/v) for 4 hours at 30°C. Following the proteolytic cleavage, pH precipitation was

employed by adding 20 mM citric acid to the protein sample. Upon precipitation, INSv was centrifuged at 3500 rpm at 4°C for 5 minutes, and the resulting pellet was dissolved in 20 mM citric acid to quench trypsin activity and subsequent removal of trypsin. After solubilization, INSv was filtered through a 0.2 μM pore diameter filter and subjected to size exclusion chromatography (SEC) using a 20 mM citric acid buffer. High-purity fractions were collected, and pH precipitation was performed using 1 M Tris, pH 10.0. The INSv pellet was then solubilized using 25 mM Tris-HCl, pH 9.0 buffer, and the concentration was adjusted to 1000 μg/mL for HDX-MS analysis.

Monomerization of commercially available insulin analog

Precipitation through pH adjustment and subsequent solubilization in 25 mM Tris-HCl pH 9.0 buffer were employed to convert IAsp (NovoRapid) from a hexameric to a monomeric state (Tokumoto et al., 2006; Fredericq, 1953). Using a 10K amicon ultrafiltration unit, a buffer exchange was performed ten times with 25 mM Tris-HCl pH 9.0. The resulting monomeric form of NovoRapid was then adjusted to a 1000 μg/mL concentration for HDX-MS analysis.

Higher-order insulin structure defined through HDX-MS analysis

HDX-MS analysis has been performed at five different time points ranging from 12 s to 24 h. Accordingly, the heat maps were generated, and the structural features based on deuterium uptake rate and electrostatic and hydrophobic potentials were visualized by *PyMOL* (DeLano, 2022). Purified INSv and IAsp were diluted in the equilibration buffer containing 50 mM Tris-HCl; pH 9.5. For labeling, 2.5 μl (≥ 35 pmol) of each sample was incubated with 37.5 μl labeling buffer containing 50 mM Tris-HCl in D_2O; pD 9.5; pH 9.1 at room temperature for 0, 0.2, 2, 20, 200, or 1440 mins incubation periods. Labeled samples were quenched with 40 μl pre-chilled quench buffer containing 50 mM Tris-HCl, 3M guanidine hydrochloride (GnHCl), 100 mM tris(2-carboxyethyl)phosphine (TCEP); pH 2.3, then the sample was incubated on ice to inhibit deuterium back-exchange. All labeling time points were subject to triplicate analyses. t_0 samples were used as reference. Relative Fractional Uptake graphs were generated by GraphPad Prism 8.1 according to uptake data obtained from *DynamX* Software (Waters Corp., 176016027).

Deuterated samples were digested using The Enzymate BEH Pepsin Column (Waters Corp., Manchester, UK) at 20°C. Upon 3 minutes of transferring digested peptides at Waters BEH C18 VanGuard trapping pre-column (flow rate 70 µl/min in 0.2% formic acid), proteins underwent online pepsin digestion and liquid chromatography/mass spectrometry (LC/MS) using the nanoACQUITY UPLC system and the Synapt G2-Si Q-Tof mass spectrometer from Waters Corp. (Milford, MA, USA). Peptide separation conditions included a 6-minute gradient with 0.2% formic acid, 35% acetonitrile, maintained at 0 °C, and a 40 µl/min flow rate. MS data were gathered using an MS^E method in resolution mode with an extended range enabled to avoid detector saturation and maintain peak morphologies (Bonn et al., 2010). MS was initially calibrated with [Glu1]-Fibrinopeptide B human (Glu-fib) peptide and MS data were gathered with lock mass correction using Glu-fib peptide in positive polarity. Peptide identification was performed by *ProteinLynx Global Server* (PLGS, 3.0.3, Waters), and identified peptides were filtered by *DynamX* Software (Waters Corp., 176016027.) according to the following parameters: minimum intensity of 800, the minimum sequence length of 3, maximum sequence length of 20, minimum products of 2, minimum products of per amino acid of 0.1, minimum score of 6, maximum MH+ error threshold of 0 ppm. Only high-quality peptides were used for analyses. Deuterium uptake was calculated by an increase in mass/charge ratio compared to t_0. *DynamX* Software generated the coverage map and heat map.

Crystallization of LysB22-AspB28 INSv insulin analog

The transformation of the INSv sample from its monomeric state to the zinc-bound form involved a zinc precipitation step using a solution comprising 2.4 M NaCl, 100 mM citric acid, and 6 mM $ZnCl_2$. Subsequently, solubilization was achieved by using 25 mM Tris-HCl solution at pH 8.0. The zinc-bound INSv samples were then screened for crystallization using the oil technique using the sitting drop vapor diffusion micro-batch. Approximately 3000 commercially available sparse matrix and grid screen crystallization conditions were employed for the initial crystallization screening. In a 72-well Terasaki plate (Cat#654,180, Greiner Bio-One, Austria), equal volumes of crystallization conditions (v/v, 0.83 µl) were mixed in a 1:1 ratio with a 5 mg/ml INSv solution. Each well was covered with 16.6 µl of paraffin oil (Cat#ZS.100510.5000,

ZAG Kimya, Türkiye) and then incubated at 4°C. Crystal formation in the wells of the Terasaki plates was observed using a compound light microscope.

Sample delivery and data collection

Data collection was performed using Rigaku's XtaLAB Synergy Flow X-ray diffraction (XRD) system, controlled by *CrysAlisPro* software (Rigaku Oxford Diffraction, 2022), following the protocol outlined in Gul et al. (2023). The airflow temperature of Oxford Cryosystems's Cryostream 800 Plus was set to 300 K (26.85 °C) and maintained consistently at ambient temperature during data collection. The 72-well Terasaki plate was mounted on the adapted XtalCheck-S plate reader attachment on the goniometer omega stage. Two dozen crystals were used for the initial screening to assess diffraction quality. Adjustments to omega and theta angles and X, Y, and Z coordinates were made to center crystals at the eucentric height of the X-ray focusing region. Subsequently, diffraction data were collected from multiple crystals. Crystals demonstrating the highest resolution Bragg diffraction peaks were chosen for further data collection, and exposure times were optimized accordingly to minimize radiation damage during overnight data collection. The most promising crystals were cultivated in a buffer solution containing 2.4 M NaCl, 100 mM Tris-HCl at pH 7.4, 6 mM $ZnCI_2$, 20 (w/v) poly(ethylene glycol) PEG-8000. Throughout the data collection process, *XtalCheck-S* was configured to oscillate to the maximum extent permitted by the detector distance, aiming to optimize crystal exposure oscillation angles. 42 frames were captured, each running lasting 3 minutes (5 seconds per frame) for all individual crystals. Parameters were set with the detector distance at 100.00 mm, a scan width of 0.5 degrees oscillation, and an exposure time of 10.00 seconds per image.

Data processing and structure determination

Following the optimization of plate screening parameters for all crystals, a 42-degree data collection was conducted for each selected crystal. All crystals were organized in *CrysAlisPro* for comprehensive data collection. An optimal unit cell was selected, and peak identification and masking procedures were executed on the collected data. Subsequently, a batch script incorporating the `xx proffitbatch` command was generated for cumulative data collection.

The batch data reduction was accomplished using the *CrysAlisPro* suite through the script command, producing files containing all integrated, unmerged, and unscaled data (*.rrpprof) for each dataset. To merge all datasets into a reflection data (.mtz) file, the *proffit merge* process in the *Data Reduction* section of the main window of *CrysAlisPro* was employed. The reduced datasets (.rrpprof files) were further merged using *proffit merge*. The entirety of the data underwent refinement, integration, and scaling processes through the aimless and pointless implementations within *CCP4* (Evans, 2014). Ultimately, the processed data were exported into *.mtz formats. The crystal structure of INSv was determined under ambient temperature within the R3:H space group, employing the automated molecular replacement tool *PHASER* integrated into the *PHENIX* software package (Adams et al., 2010). Utilizing a previously published X-ray structure (PDB ID: 4GBN) (Palmieri et al., 2013) as the initial search model, the coordinates from 4GBN were employed for the preliminary rigid-body refinement within *PHENIX*. Subsequent refinement steps included simulated-annealing refinement, adjustment of individual coordinates, and Translation/Libration/Screw (TLS) parameters. Furthermore, a refinement technique known as composite omit map, embedded in *PHENIX*, was executed to identify potential locations of altered side chains and water molecules. The final model underwent meticulous examination and model-building in *COOT*, focusing on positions exhibiting notable difference density. Extraneous water molecules located beyond regions of significant electron density were manually excluded. The X-ray crystal structure was visualized using *PyMOL* and *COOT* (Emsley et al., 2004).

Differential Scanning Calorimetry

Differential scanning calorimetry (DSC) was conducted to assess the thermal stability of aspart and INSv insulin samples at a 2 mg/ml concentration, employing a SETARAM Micro DSC-III calorimeter (Jandel Scientific). The measurements were carried out within the 20 to 100°C temperature range, employing a heating rate of 0.3 K/min. Precision balancing, with an accuracy of ± 0.05 mg, was employed for the aspart and INSv samples and the reference (20 mM citric acid buffer solution) to mitigate corrections involving the heat capacity of the vessels. A secondary thermal scan of the denatured sample was performed for baseline correction. Analysis of the melting temperature (T_m), calculation of calorimetric enthalpy (ΔH_{cal}), and determination

of the change in entropy (ΔS) were executed using the Origin® 2021 software (OriginLab Corporation, Northampton, USA).

Gaussian Network Model with All Cα in the Structures

We conducted normal mode analysis using ProDy (Bakan et al., 2011). Specifically, we employed the Gaussian Network Model (GNM) analysis for the newly determined INSv structure at ambient temperature and a previously resolved structure at cryogenic conditions (PDB ID: 4GBN). Contact maps were defined based on all Cα atoms, utilizing a cutoff distance of 8.0 Å. N − 1 nonzero normal modes were derived, where N represents the total number of Cα atoms. For each structure, we calculated squared fluctuations over the weighted 10 slowest and 10 fastest modes, enabling a comparison of their global and local motions, respectively.

Results

R→K substitution on insulin AspB28 (INSv)

To enhance the flexibility of IAsp, we introduced a substitution from arginine (Arg) to lysine (Lys) in chain B. The internal Arg22 on IAsp was specifically mutated to Lys to mitigate the formation of undesired cleavage products, as trypsin exhibits a higher affinity for Arg than Lys. DSC measurements were conducted to investigate the thermal stability of the INSv (LysB22-AspB28) compared to commercially available IAsp (AspB28). DSC measurements revealed significant differences in the thermodynamic properties of IAsp and INSv (Fig. 1). The thermal unfolding of IAsp shows a steep endothermic denaturation with a T_m of 81.9 °C, a ΔH_{cal} of 35.46 KJ/mol, and a ΔS of 0.099 KJ/mol·K. On the other hand, the T_m of the INSv was considerably lower (T_m = 77.6 °C), and the ΔH_{cal} also decreased (ΔH_{cal}= 31.55 KJ/mol), as well as the ΔS showed increasing tendency (ΔS= 0.142 KJ/mol·K). The significantly lower T_m suggests a less stable and, most likely, less compact conformation for the INSv. Moreover, the decreased ΔH_{cal}

and increased ΔS of INSv align with the lower T_m, assuming the protein conformation is more flexible.

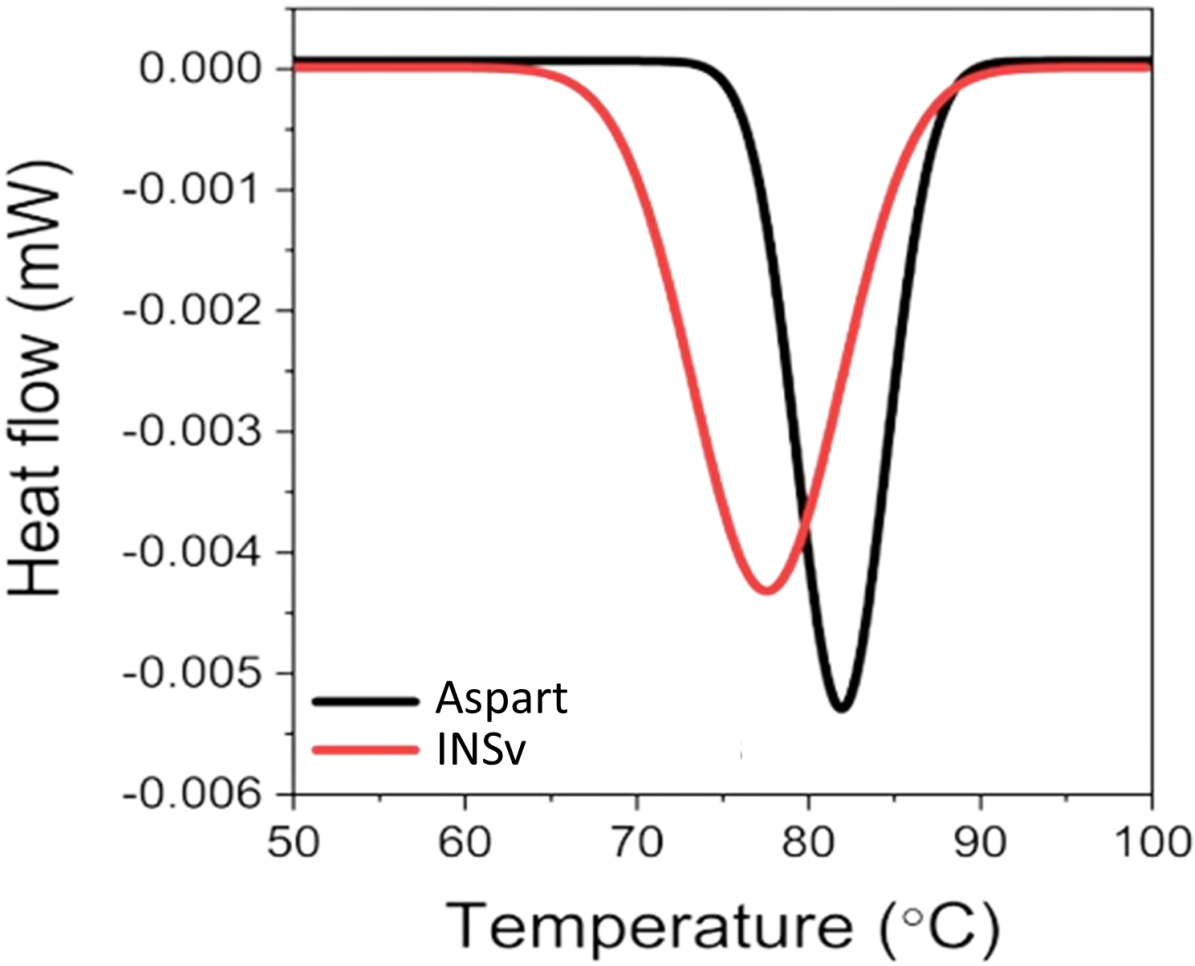

Figure 1. Differential scanning calorimetry analysis of AspB28 (IAsp) and LysB22-AspB28 (INSv) analogs. The variation in heat flow depends on the melting temperature (T_m), which signifies the point at which 50% of the protein undergoes denaturation. Furthermore, the calorimetric enthalpy (ΔH_{cal}) was computed, and the alteration in conformational entropy (ΔS) was ascertained by evaluating the ratio of ΔH_{cal} to T_m in Kelvin (K).

Crystal structure of novel insulin LysB22-AspB28 (INSv) crystal form

We determined the ambient temperature structure of INSv at 2.5 Å resolution. There are two nearly identical monomer molecules within the asymmetric unit cell exhibiting an overall RMSD of 0.81 Å. Superpositioning and comparative analysis with the PDB structure of 4GBN revealed

overall RMSD values ranging from 0.3 Å to 0.83 Å for the nearly identical monomer molecules in the asymmetric unit. Molecular replacement with a dimer in the asymmetric unit facilitated the solution of the crystal structures of INSv insulin at pH 7.5. Specifically, amino acid residues 1 to 8 exhibited a "T" conformation in one monomer and an "R" conformation in the other with well-defined electron densities (Fig. 2). In the previously reported IAsp structure (PDB_ID: 4GBN), three symmetry-related "TR" dimers constituted the biological unit (Palmieri et al., 2013). The hexameric configuration of INSv is organized near a crystallographic 3-fold axis aligned with the central channel (Palmieri et al., 2013). In contrast to the 4GBN structure, a distinctive feature of the INSv hexamer involves the outward orientation of Asn3 in chain B relative to the interior of the channel (Fig 2A-B). This spatial arrangement produces less stable electrostatic interaction with the two symmetry-related B3Asn residues (Fig. 2). The crystal structures of INSv and 4GBN exhibit similarities in both Cα atoms and side chains. Although there are positional variations, these are primarily minor, with relatively major discrepancies observed in the side chains of 4GBN (Palmieri et al., 2013) IAsp compared to INSv. Upon superimposing the current INSv insulin structure onto 4GBN in the T_3R_3 conformation, a dissimilarity becomes evident in the region encompassing amino acid residues 1 to 8 in chain B. This dissimilarity is observed in both backbone and side chain conformations, providing evidence for INSv insulin adopting the T_3R_3 conformation with a pure TR-state dimer configuration. A pairwise global structural alignment between the T_3R_3-INSv and -4GBN IAsp structures highlights their similarity, with a global RMSD slightly over 0.8 Å. This similarity persists, indicating a consistent outcome attributable to the zinc-bound form.

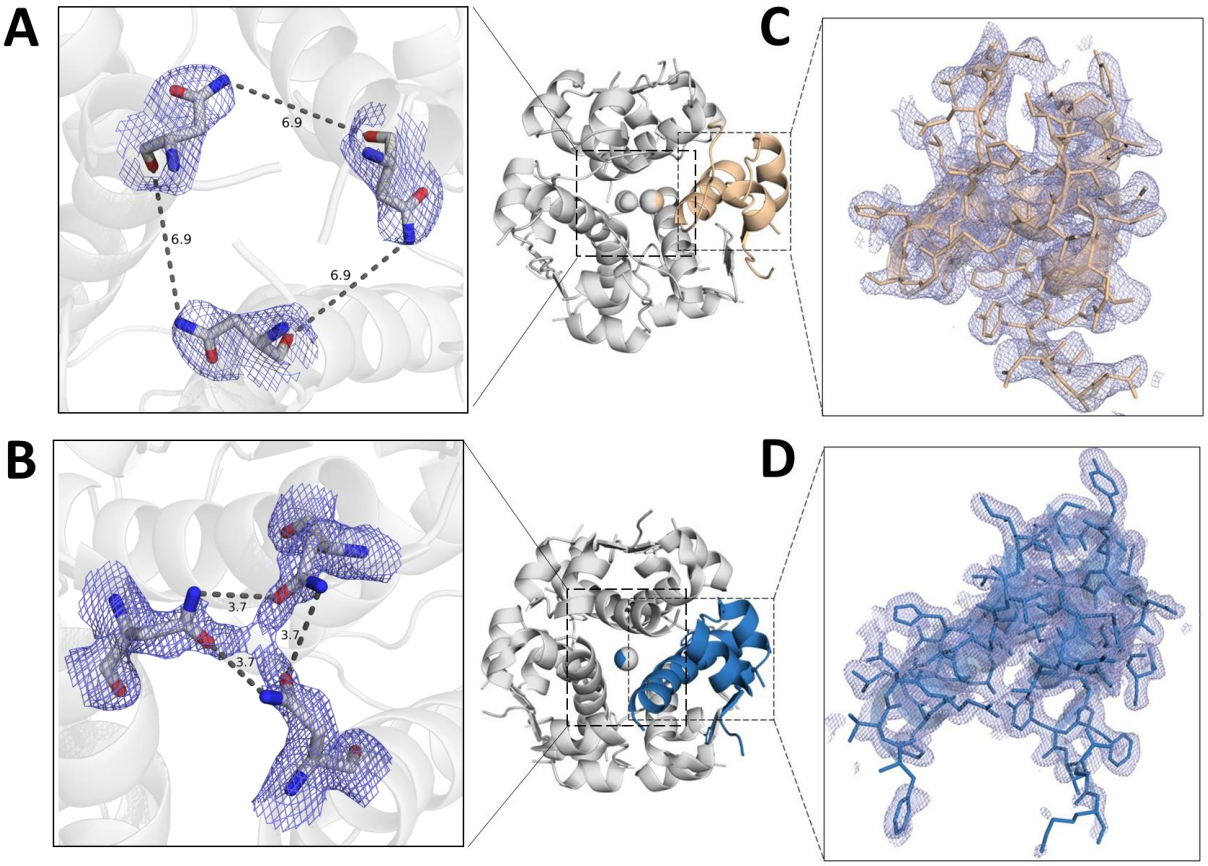

Figure 2. A comparison between the INSv and 4GBN IAsp structures, presenting both distant and close-up views. Panels (A) and (B) depict the electrostatic interaction distances of AsnB3 residues within each monomer of insulin hexamers, INSv and 4GBN, respectively. Additionally, panels (C) and (D) provide a close-up examination of a monomer from insulin hexamers INSv and 4GBN, respectively. 2*Fo-Fc* simulated annealing-omit map at 1 sigma level is colored in slate.

We conducted a separate B-factor analysis for the monomers of 4GBN and INSv (Fig. 3). In the R-forms of the INSv and 4GBN IAsp structures, it is observed that the N-terminal segments ranging from Asn21-Gln25 and Gly41-Glu42 of INSv's B chain exhibit slightly higher fluctuations compared to their counterparts in the 4GBN IAsp structure. Similarly, in the T-forms of the INSv and 4GBN IAsp structures, the regions spanning Cys40-Glu42 in INSv demonstrate pronounced flexibility relative to the T-form of the 4GBN IAsp structure. This implies that the T-forms exhibit greater fluctuation than the R-form. Additionally, substituting R with K might induce a flexible state despite the limited influence of Zn^{+2} coordination on the hexameric form.

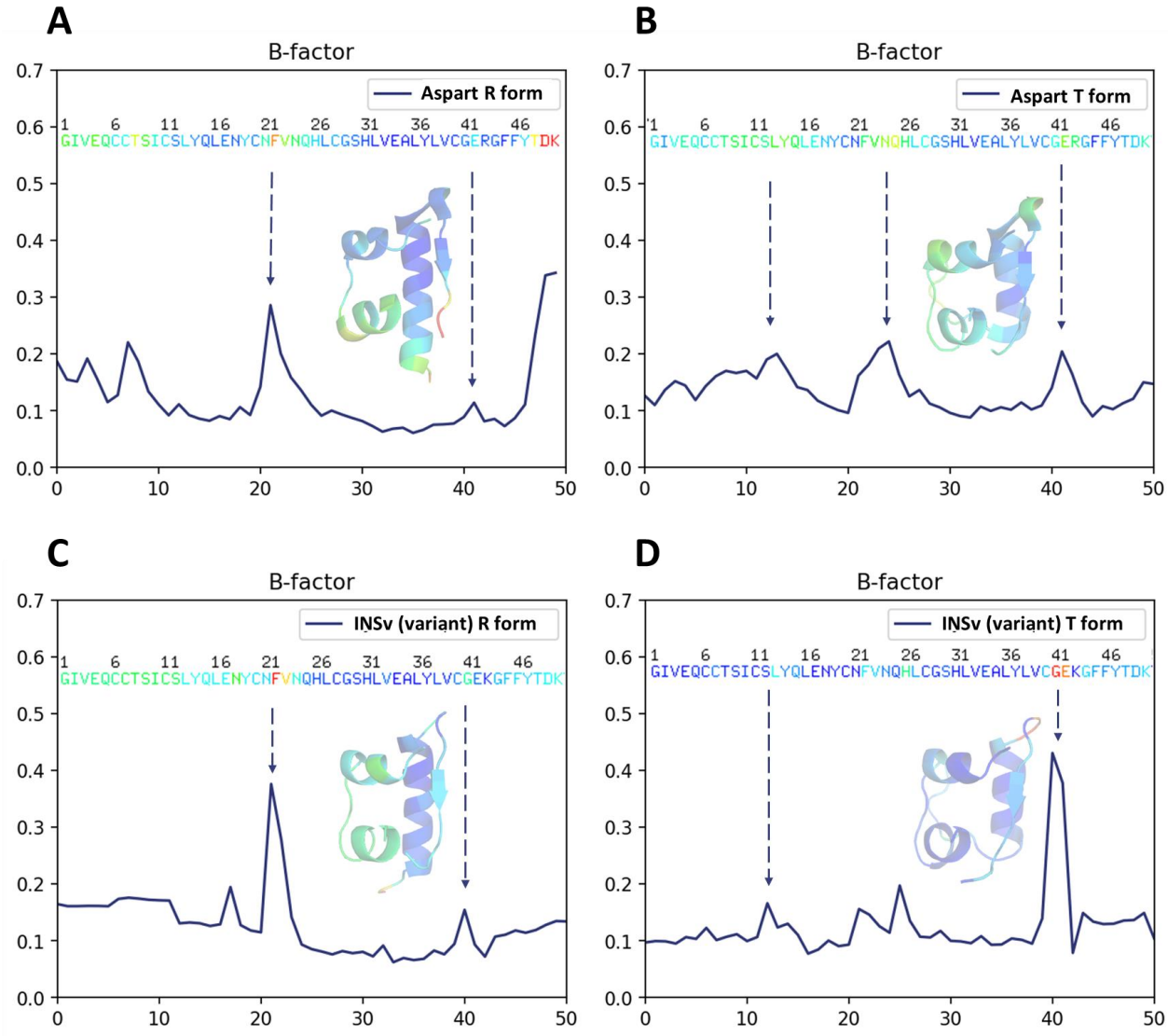

Figure 3. Experimental B-factor analysis and cartoon representation of each 4GB IAsp and INSv dimers' monomer. (A, B) Thermal distance analysis supports the experimental b-factor of the IAsp structure's R-state and T-state conformers. (C, D) Thermal distance analysis supports the experimental b-factor of the INSv structure's R state and T state conformer. Cartoon mode is colored by the B-factor in *PyMOL*. The blue spectrum indicates areas of rigidity, whereas the red spectrum indicates regions of flexibility.

Alternate dynamics status in AspB28 (IAsp) and LysB22-AspB28 (INSv) monomers

In this study, we quantified deuterium exchange in distinct regions of INSv and IAsp, identified the locations of disparities, and elucidated the variations in their local dynamics. In conducting HDX-MS reactions, we specifically opted for the monomeric form of insulins to determine

differences in monomer dynamics under identical experimental conditions. Consequently, even if substantial dynamic differences were not observed in the mutated region of these insulins, notable differences were noted in the dynamics of the remaining monomeric regions (Fig. 4A). In alignment with the dynamic behaviors of the structures, we identified electrostatic and hydrophobic distinctions (Fig. 4B).

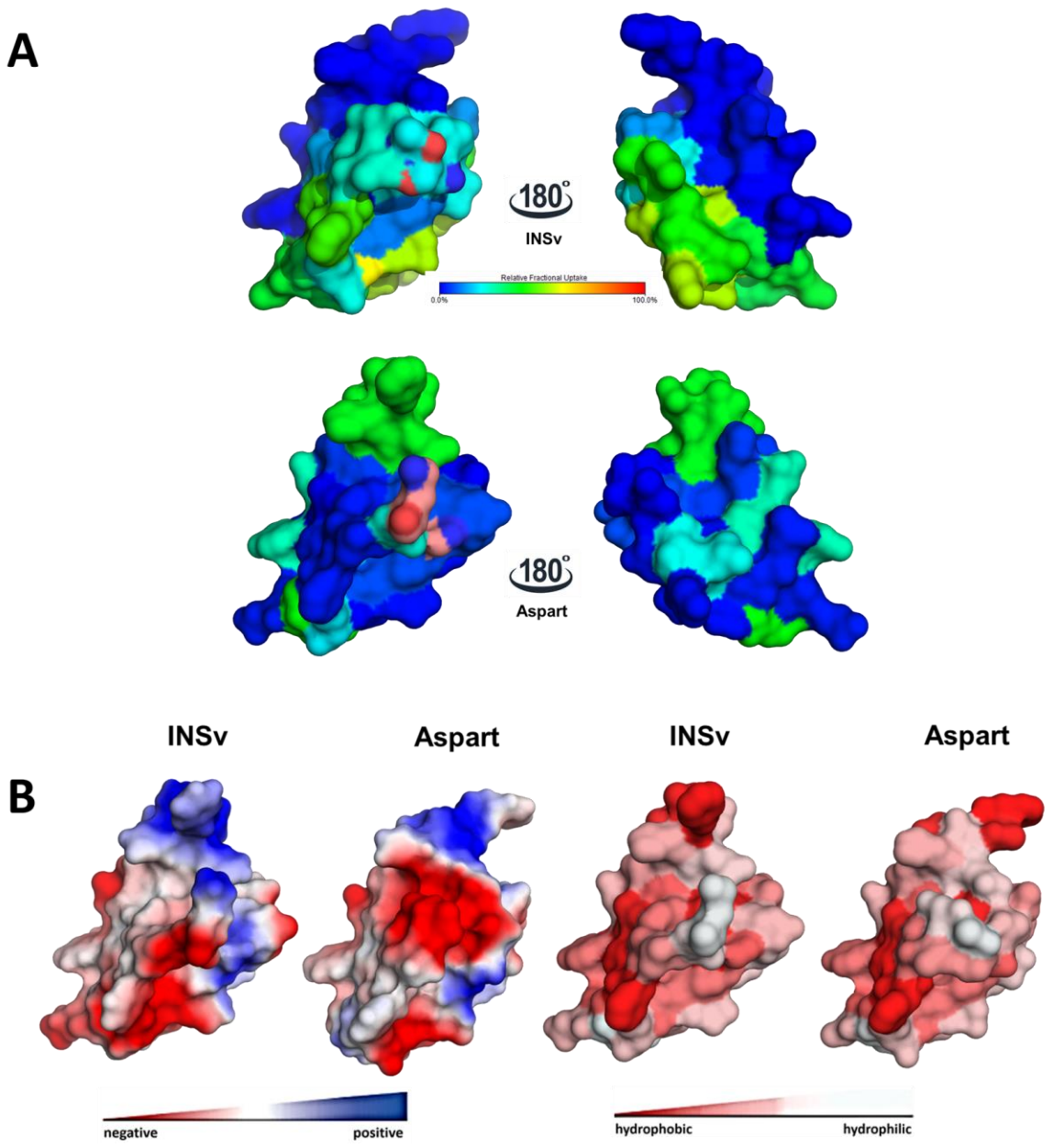

Figure 4. The surface features of INSv and 4GBN IAsp. (A) Visualization of deuterium exchange over 1440-minute intervals through aligning our newly determined monomer of INSv with the monomer of 4GBN IAsp. The blue spectrum marks the areas of rigidity, whereas the red spectrum indicates regions of flexibility. (B) Illustration of electrostatic potential and hydrophobicity of INSv and 4GBN structures. Figures have been generated by *PyMOL*.

Initially, to ensure uniformity in pH conditions during the exchange reaction, Tris-HCl buffer at pH 9.1 (pD 9.5) was selected, owing to its ability to maintain insulin's *in vivo* monomeric state (REF). The temporal evolution of deuterium exchange profiles by IAsp is indicated in Figure 5. In the H/D exchange reaction of the IAsp monomer, certain residues, namely regions involving Cys11-Leu13, Asn21-Cys28, Glu34-Tyr37, Arg43-Gly44, and Asp49, exhibit a notable degree of deuterium exchange indicating relatively more mobile compared to other residues (Fig. 5A), consistent with findings from computational analyses (Fig. 5B). Our normal mode analysis identifies Ile2, Cys6, Ile10, Gln15-Leu16, Asn18-Tyr19, Leu27-Cys28, Glu34-Leu36, Leu38-Val39, and Arg43-Gly44 as regions undergoing dynamic dissections, and these are referred to as kinetically hot regions (Fig. 5B). These identified hinge sites from our computational analysis corroborates with observations in the HDX-MS heat-map results. However, Ser12 and Gln15-Leu16 residues are identified as crucial hinge regions in only GNM analysis (Fig. 5B).

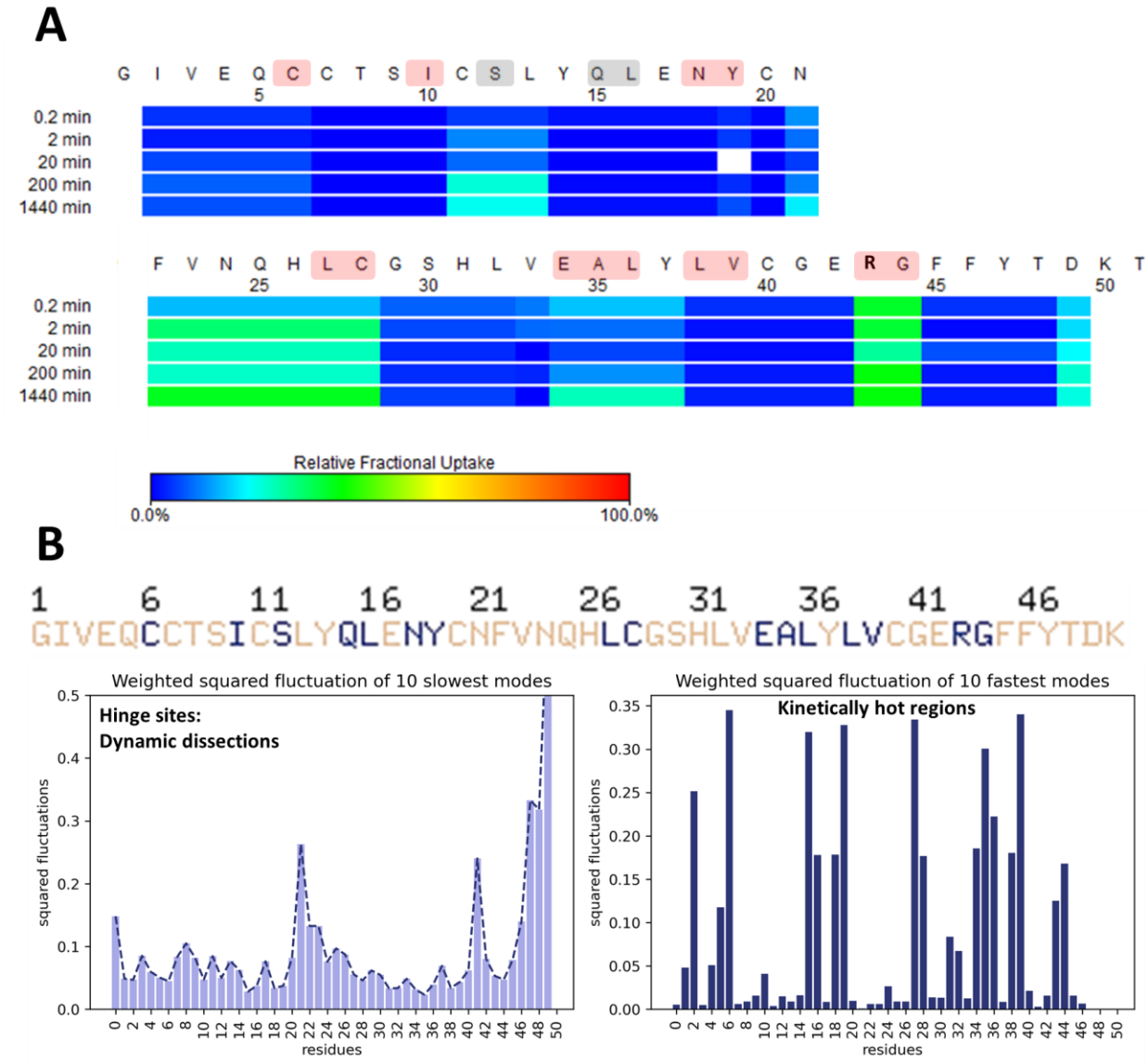

Figure 5. Complementary experimental and computational dynamic analysis of IAsp. (A) Heat map displaying time-course H/D exchange measurements of IAsp. The color code from blue to red describes deuterium exchange. (B) Cumulative 10 slowest and 10 fastest modes from GNM to show dynamic dissections and kinetically hot regions. The critical residues for relative fractional deuterium exchange, which are highlighted in red, are largely consistent with the cumulative 10 slowest and 10 fastest modes from GNM. The residues observed in the H/D reaction alone are illuminated in gray.

Next, the H/D exchange reaction in INSv insulin analog was compared to IAsp to assess potential distinctions. The INSv analog demonstrated higher deuterium exchange compared to IAsp (after a 1440-minute reaction, n = 3), displaying a more dynamic conformation for INSv

analog compared to IAsp, agreeing with the findings of DSC analysis (Fig. 6A). Within the H/D exchange reaction of the INSv monomer, specific regions, Ile2-Cys6, Ser9-Asn18, Cys20-Asn21, and Val39-Asp49, exhibited a noticeable degree of relative mobility in contrast to other residues, broadly consistent with computational analyses (Fig. 6A). Our normal mode analysis identified Glu4-Cys6, Ser9-Ile10, Asn18-Tyr19, His31-Leu32, and Val39 residues as regions undergoing dynamic dissections, denoted as kinetically hot regions (Fig. 6B). Notably, the identified hinge sites from our computational analysis align seamlessly with observations in the HDX-MS heat-map results. Nevertheless, Ala35-Leu36 and Gly44 residues consistently emerged as crucial hinge regions only in our GNM analysis (Fig. 6B).

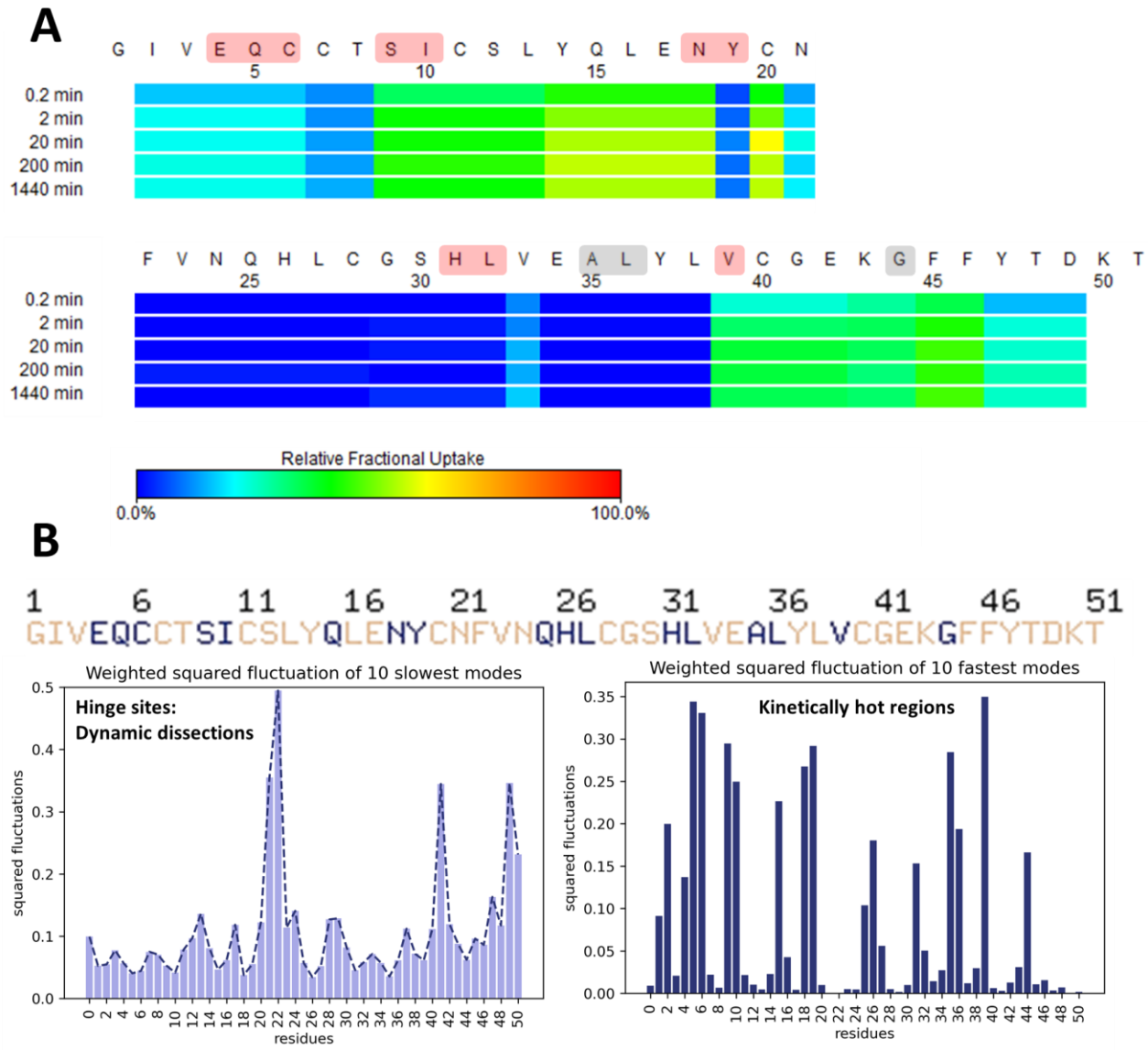

Figure 6. Complementary experimental and computational dynamic analysis of INSv. (A) Heat map displaying time-course H/D exchange measurements of INSv. (B) Cumulative 10 slowest and 10 fastest modes from GNM to show dynamic dissections and kinetically hot regions. The critical residues for relative fractional deuterium exchange, which are highlighted in red, are largely consistent with the cumulative 10 slowest and 10 fastest modes from GNM. The residues observed in the HDX reaction alone are illuminated in gray in panel A.

Figure 7A depicts the close-up view of deuteration levels of the corresponding fragments of INSv and IAsp over the 200-minute time course. The uptake profiles of most fragments exhibited variations between INSv and IAsp (Fig. 7A-B). Additionally, there was a minimal

resemblance in the fragment encompassing His31-Asp49, which includes the mutation site in INSv (Fig. 7B).

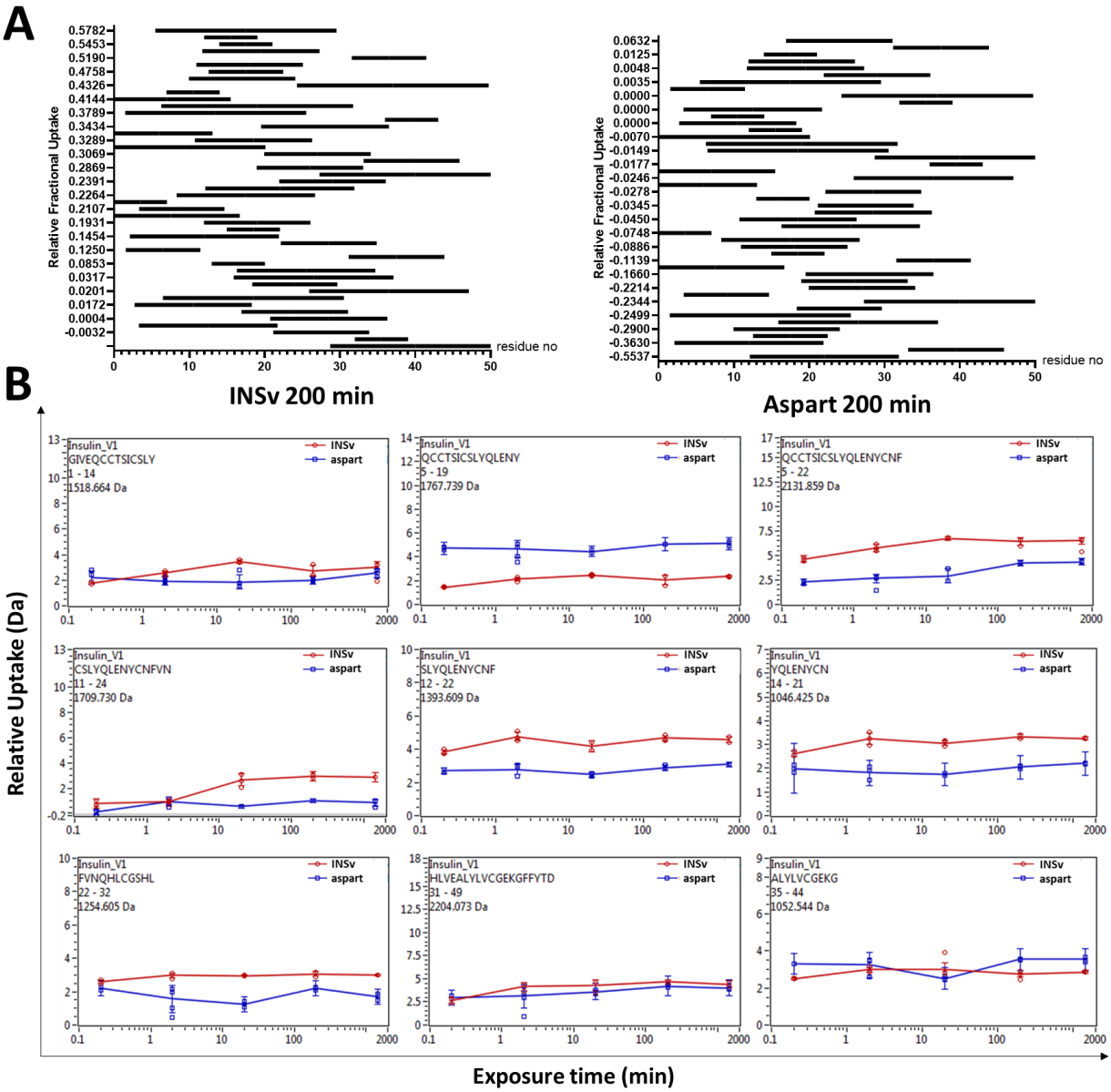

Figure 7. Projection of the peptide-specific deuterium exchange. (A) Relative deuterium exchange of INSv and IAsp peptides depicted by Woods plots over the 200 min time course. (B) Comparison between time-dependent relative deuterium exchange of representative INSv and IAsp peptides. Data is represented on a logarithmic scale.

Discussion

Zinc^{+2}-coordinated hexameric form of insulins exemplifies characteristic structural features inherent in globular proteins (Chothia et al., 1983). Serving as a pivotal model in the evolution and application of X-ray crystallographic techniques (Baker et al., 1988), the hexamer functions as a stable reservoir of the hormone within both the secretory granules of pancreatic β-cells and pharmaceutical formulations (Brange et al., 2012). The integration of structure-based mutagenesis into the Zn^{+2}-bound insulin hexamer (Brange et al., 2012; Dodson and Steiner, 1998) has significantly advanced the development of rapid-acting insulin analog formulations suitable for prandial injection and pump use (Zinman et al., 1997). Despite their initial categorization as "monomeric"(Brange et al., 2012), these analogs are presently designed either as Zn^{+2}-bound insulin hexamers or as an equilibrium distribution of Zn^{+2}-free oligomers (DeFelippis et al., 2001; Garg et al., 2005). The overarching objective of this protein engineering endeavor was to optimize glycemic control while mitigating the risk of major hypoglycemic events per decrement in hemoglobin A1c (Renner et al., 1999; Melki et al., 1998; Hartemann-Heurtier et al., 2003). Although insulin analogs represent a significant advancement in the pharmacotherapy of diabetes and rapid-acting insulins offer specific benefits compared to regular insulin, a requirement still exists to formulate ultrafast-acting insulin preparations, closely emulating the physiological release of insulin (Kalra and Gupta, 2014).

The present study has explored the examination of the INSv alongside the IAsp to illuminate the fundamental structure and dynamics of monomeric rapid-acting insulin in a solution. The substitution of Arg with Lys at position B22 and Pro with Asp at position B28 distinguish the INSv, which DSC confirmed to be a less stable insulin analog. Lys and Arg, both positively charged basic amino acids under physiological conditions, are predominantly exposed on the surfaces of proteins (Galligan et al., 2017; Li et al., 2013; Warwicker et al., 2014). Despite their shared function as basic residues, Arg contributes more stability to protein structure than Lys, attributed to its distinctive geometric structure (Sokalingam et al., 2012). The guanidinium group in Arg facilitates interactions in three possible directions over its three asymmetrical nitrogen atoms (Nη1, Nη2, Nε). In contrast, the basic functional group of Lys allows interaction in only one direction (Xu et al., 2017; Malinska et al., 2016; Wu et al., 2016). This capability enables

Arg to form more electrostatic interactions, including salt bridges and hydrogen bonds, than lysine. Presumably, this results in stronger interactions than those generated by Lys.

Based on the compatibility between the experimental B-factor analysis and the H/D exchange reaction of INSv (Fig. 3 and Fig. 6), the solution structure of this variant closely mirrors the crystallographic R state. However, unlike the IAsp structure, a distinct feature of the INSv hexamer in the R form involves the outward orientation of Asn3 in chain B relative to the interior of the channel. This spatial configuration leads to a less stable electrostatic interaction with the two symmetry-related AsnB3 residues. Additionally, the unique R-state of the INSv crystal structure is evident in a flexible INSv monomer according to B-factor analysis (Fig. 3), which correlates with the HDX-MS findings for the INSv monomer (Fig. 6). Characterizing INSv and IAsp as native-like monomers at pH 9.0 (Tokumoto et al., 2006; Fredericq, 1953; Kadima et al., 1992;) and without an organic co-solvent provides an opportunity for a quantitative assessment of amide-proton exchange in D_2O. HDX-MS data for INSv indicated swift deuterium exchange at the initial time points in the majority of peptides, followed by local exchange after specific time points (Fig. 6A). In contrast, IAsp exhibited no deuterium exchange in the first 35 residues, with only the Phe22-Cys28 and Arg43-Gly44 peptides showing deuterium exchange and local exchange at 2-min, 20-min, 200-min and 1440-min points (Fig. 5A).

The formation of insulin oligomers primarily relies on establishing noncovalent bonds between interacting residues from adjacent monomers (Dunn, 2005). However, alterations in pH can interrupt these interactions, causing residues in distant sites to cease their communication paths and transition into monomeric states (Fredericq, 1953; Tokumoto et al., 2006). Modifying monomeric states results in substantial modifications to the customary residue communication network compared to oligomeric states (Bolli et al., 2000; Eren et al., 2021). These alterations can also be elucidated through computational GNM analysis (Tandon et al., 2021; Sorkina et al., 2021), which is analogous to our insights from experimental H/D exchange reactions (Fig. 5B and Fig. 6B). We conducted GNM in this study to further elucidate the distinctive dynamics exhibited by the INSv monomer compared to the monomeric form of IAsp, aiming to correlate HDX-MS results. The monomeric IAsp (NovoRapid) was employed as the reference model, which is analogous to the methodology used in HDX-MS. GNM-based methodologies precisely assess global protein motions at lower frequencies and local motions at higher frequencies (Eren

et al., 2021). In the INSv monomer, pivotal hinge sites crucial for insulin activity are identified in residues Cys6, Ser9, Asn18-Tyr19, and Leu32, as observed through GNM and HDX-MS analyses (Fig. 6B). Conversely, in the IAsp monomer, hinge sites critical for insulin activity are in Cys6, Ile10, Asn18-Tyr19, Cys28, Glu34, Leu38, and Arg43-Gly44 (Fig. 5B). Remarkably, these residues (in Fig. 5B and Fig. 6B) exhibiting dynamic changes are the regions involved in receptor interactions (De Meyts, 2000). The dynamic variations observed, both experimentally and computationally, suggest that while the hexameric structure bound to Zn^{+2} cation may not change significantly, the substitution of Arg with Lys in a monomer induces distinct kinetic models dependent on particular mobilities. Considering the tendency of conformational fluctuations to hasten the degradation of pharmaceutical formulations, we propose that adopting a concept referred to as 'dynamic restructuring' for insulin could enable the strategic development of formulations with ultrafast action, given the observed kinetic differences.

Conclusion

In this study, we introduced a less stable monomeric insulin variant, INSv. The crystal structure of its hexameric insulin variant was determined at a resolution of 2.5 Å at ambient temperature. A H/D exchange dynamic between the IAsp and the INSv revealed that INSv exchanges deuterium atoms more rapidly and extensively than intact IAsp, which is consistent with the diminished hexameric stability of INSv. GNM analysis further supported these kinetic differences. The observed variations prompted exploring the specific regions responsible for both molecules' discrepant H/D exchange reactivity. These deuteration discrepancies, coupled with computational analysis, imply that the R→K substitution can induce distinct kinetic models, even under identical physiological conditions.

Ethics approval and consent to participate

Not applicable.

Consent for publication

Not applicable.

Availability of data and materials

Not applicable.

Competing interests

The authors declare that they have no competing interests.

Funding

E.T. was supported by the University of Pécs Medical School, a grant from Dr. Szolcsányi János Research Fund (KA-2022-09), as well as the grant of Dr. Romhányi György fellowship for young scientists (ÁOK-IK). This research was financially supported by The Scientific and Technological Research Council of Turkey (TUBITAK) (Project no: 122R061). E.A. was supported by received funding from the TUBITAK 2244 Program. Additionally, M.T. and B.D. received funding from the TUBITAK 2211 Program.

Authors' contributions

E.A., H.D., and G.D.D. designed the experiments. E.A. prepared the samples. E.A. performed the sample delivery, data collection, and data processing. Structures were refined by E.A. DSC analysis was performed by E.T. HDX-MS analysis was performed by M.T., O.T., E.A., and B.D. GNM analysis was performed by E.A. The manuscript was prepared by E.A., M.T., O.T., E.T., B.D., G.D.D., and H.D.

Acknowledgment

The authors thank Dr. İrfan Çinkaya for his invaluable support. The authors gratefully acknowledge the use of the services and facilities of the Istanbul Technical University MOBGAM (Molecular Biology-Biotechnology&Genetics Research Center), University of Health Science-Validebag DETAUM (Experimental Medicine Research and Application Center), and DEVA Holding A.Ş.

References

Adams, P. D., Afonine, P. V., Bunkóczi, G., Chen, V. B., Davis, I. W., Echols, N., Headd, J. J., Hung, L. W., Kapral, G. J., Grosse-Kunstleve, R. W., McCoy, A. J., Moriarty, N. W., Oeffner, R., Read, R. J., Richardson, D. C., Richardson, J. S., Terwilliger, T. C., & Zwart, P. H. (2010). PHENIX: A comprehensive Python-based system for macromolecular structure solution. *Acta Crystallographica Section D: Biological Crystallography*. doi: 10.1107/S0907444909052925

Avgerinos, I., Papanastasiou, G., Karagiannis, T., Michailidis, T., Liakos, A., Mainou, M., Matthews, D. R., Tsapas, A., & Bekiari, E. (2021). Ultra-rapid-acting insulins for adults with diabetes: A systematic review and meta-analysis. *Diabetes, Obesity and Metabolism*. doi: 10.1111/dom.14461

Bakan, A., Meireles, L. M., & Bahar, I. (2011). ProDy: Protein dynamics inferred from theory and experiments. *Bioinformatics*. doi: 10.1093/bioinformatics/btr168

Baker, E. N., Blundell, T. L., Cutfield, J. F., Cutfield, S. M., Dodson, E. J., Dodson, G. G., Hodgkin, D. M., Hubbard, R. E., Isaacs, N. W., & Reynolds, C. D. (1988). The structure of 2Zn pig insulin crystals at 1.5 A resolution. *Philosophical Transactions of the Royal Society of London. Series B, Biological Sciences*, *319*(1195), 369–456. doi: 10.1098/RSTB.1988.0058

Bolli, G. B., & Owens, D. R. (2000). Insulin glargine. In Lancet. doi: 10.1016/S0140-6736(00)02546-0

Bonn, B., Leandersson, C., Fontaine, F., & Zamora, I. (2010). Enhanced metabolite identification with MSE and a semiautomated software for structural elucidation. *Rapid Communications in Mass Spectrometry*. doi: 10.1002/rcm.4753

Brange, J. (2012). *Galenics of insulin: the physico-chemical and pharmaceutical aspects of insulin and insulin preparations*. Retrieved from https://books.google.com/books?hl=tr&lr=&id=EGnmCAAAQBAJ&oi=fnd&pg=PA1&dq=Brange,+J.,+Skelbaek-Pedersen,+B.,+Langkjaer,+L.,+Damgaard,+U.,+Ege,+H.,+Havelund,+S.,+Heding,+L.+G.,+Jorgensen,+H.,+Lykkeberg,+J.,+Markussen,+M.,+Pingel,+M.,+and+Rasmussen,+E.+(1987).+Galenics+of+Insulin:+The+Physico-Chemical+and+Pharmaceutical+Aspects+of+Insulin+and+Insulin+Preparations.+Berlin:+Springer-Verlag.&ots=8UuCj-8jeH&sig=TmIUoblxeG9RtC1X6i0nyHdUyNk

Chothia, C., Lesk, A. M., Dodson, G. G., & Hodgkin, D. C. (1983). Transmission of conformational change in insulin. *Nature*. doi: 10.1038/302500a0

De Meyts, P. (2000). The Insulin Receptor and Its Signal Transduction Network. In Endotext.

DeFelippis, M. R., Chance, R. E., & Frank, B. H. (2001). Insulin self-association and the relationship to pharmacokinetics and pharmacodynamics. In Critical Reviews in Therapeutic Drug Carrier Systems. doi: 10.1615/critrevtherdrugcarriersyst.v18.i2.30

Delano, W. L. (2002). The PyMOL Molecular Graphics System. *CCP4 Newsletter on Protein Crystallography*.

Dodson, G., & Steiner, D. (1998). The role of assembly in insulin's biosynthesis. *Current Opinion in Structural Biology*. doi: 10.1016/S0959-440X(98)80037-7

Dunn, M. F. (2005). Zinc-ligand interactions modulate assembly and stability of the insulin hexamer - A review. *BioMetals*. doi: 10.1007/s10534-005-3685-y

Dutta, D., Mohindra, R., Mahajan, K., & Sharma, M. (2023). Performance of Fast-Acting Aspart Insulin as Compared to Aspart Insulin in Insulin Pump for Managing Type 1 Diabetes Mellitus: A Meta-Analysis. *Diabetes and Metabolism Journal*. doi: 10.4093/dmj.2022.0035

Emsley, P., & Cowtan, K. (2004). Coot: Model-building tools for molecular graphics. *Acta Crystallographica Section D: Biological Crystallography*. doi: 10.1107/S0907444904019158

Eren, M., Tuncbag, N., Jang, H., Nussinov, R., Gursoy, A., & Keskin, O. (2021). Normal Mode Analysis of KRas4B Reveals Partner Specific Dynamics. *Journal of Physical Chemistry B*. doi: 10.1021/acs.jpcb.1c00891

Evans, P. (2014). CCP4 Tools for X-ray Integration and Data Processing. *Nihon Kessho Gakkaishi*. doi: 10.5940/jcrsj.56.s24

Fredericq, E. (1953). Reversible dissociation of insulin [10]. In Nature. doi: 10.1038/171570a0

Galligan, J. J., Kingsley, P. J., Wauchope, O. R., Mitchener, M. M., Camarillo, J. M., Wepy, J. A., Harris, P. S., Fritz, K. S., & Marnett, L. J. (2017). Quantitative analysis and discovery of lysine and arginine modifications. *Analytical Chemistry*. doi: 10.1021/acs.analchem.6b04105

Garg, S. K., Ellis, S. L., & Ulrich, H. (2005). Insulin glulisine: A new rapid-acting insulin analogue for the treatment of diabetes. In Expert Opinion on Pharmacotherapy. doi: 10.1517/14656566.6.4.643

Gul, M., Ayan, E., Destan, E., Johnson, J. A., Shafiei, A., Kepceoğlu, A., Yilmaz, M., Ertem, F. B., Yapici, İ., Tosun, B., Baldir, N., Tokay, N., Nergiz, Z., Karakadioğlu, G., Paydos, S. S., Kulakman, C., Ferah, C. K., Güven, Ö., Atalay, N., … DeMirci, H. (2023). Rapid and efficient ambient temperature X-ray crystal structure determination at Turkish Light Source. *Scientific Reports*. doi: 10.1038/s41598-023-33989-0

Hartemann-Heurtier, A., Sachon, C., Masseboeuf, N., Corset, E., & Grimaldi, A. (2003). Functional intensified insulin therapy with short-acting insulin analog: Effects on HbA1c and frequency of severe hypoglycemia: An observational cohort study. *Diabetes and Metabolism*. doi: 10.1016/S1262-3636(07)70007-1

Heise, T., Hövelmann, U., Brøndsted, L., Adrian, C. L., Nosek, L., & Haahr, H. (2015). Faster-acting insulin aspart: Earlier onset of appearance and greater early pharmacokinetic and pharmacodynamic effects than insulin aspart. *Diabetes, Obesity and Metabolism*. doi: 10.1111/dom.12468

Home, P. D. (2012). The pharmacokinetics and pharmacodynamics of rapid-acting insulin analogues and their clinical consequences. In Diabetes, Obesity and Metabolism. doi: 10.1111/j.1463-1326.2012.01580.x

Hsu, L., Buckingham, B., Basina, M., Ekhlaspour, L., Von Eyben, R., Wang, J., & Lal, R. A. (2020). Fast-Acting Insulin Aspart Use with the MiniMedTM 670G System. *Https://Home.Liebertpub.Com/Dia*, *23*(1), 1–7. doi: 10.1089/DIA.2020.0083

Kadima, W., Roy, M., Lee, R. W. K., Kaarsholm, N. C., & Dunn, M. F. (1992). Studies of the association and conformational properties of metal-free insulin in alkaline sodium chloride solutions by one- and two-dimensional 1H NMR. *Journal of Biological Chemistry*. doi: 10.1016/s0021-9258(19)50374-x

Khosravi, F., Upadhyay, M., Kumar, A., Shahsavani, M. B., Akbarian, M., Najafi, H., Tamaddon, A. M., & Yousefi, R. (2022). A novel method for the chaperone aided and efficient production of human proinsulin in the prokaryotic system. *Journal of Biotechnology*. doi: 10.1016/j.jbiotec.2022.01.002

Kim, C. K., Lee, S. B., & Son, Y. J. (2015). Large-scale refolding and enzyme reaction of human preproinsulin for production of human insulin. *Journal of Microbiology and Biotechnology*. doi: 10.4014/jmb.1504.04062

Li, L., Vorobyov, I., & Allen, T. W. (2013). The different interactions of lysine and arginine side chains with lipid membranes. *Journal of Physical Chemistry B*. doi: 10.1021/jp405418y

Malinska, M., Dauter, M., & Dauter, Z. (2016). Geometry of guanidinium groups in arginines. *Protein Science*. doi: 10.1002/pro.2970

Melki, V., Renard, E., Lassmann-Vague, V., … S. B.-D., & 1998, undefined. (1998). Improvement of HbA1c and Blood Glucose Stability in IDDM Patients Treated With Lispro Insulin Analog in External Pumps. *Am Diabetes AssocV Melki, E Renard, V Lassmann-Vague, S Boivin, B Guerci, H Hanaire-Broutin, J BringerDiabetes Care, 1998•Am Diabetes Assoc*. doi: 10.2337/diacare.21.6.977

Min, C. K., Son, Y. J., Kim, C. K., Park, S. J., & Lee, J. W. (2011). Increased expression, folding and enzyme reaction rate of recombinant human insulin by selecting appropriate leader peptide. *Journal of Biotechnology*. doi: 10.1016/j.jbiotec.2010.12.023

Palmieri, L. C., Fávero-Retto, M. P., Lourenço, D., & Lima, L. M. T. R. (2013). A T3R3 hexamer of the human insulin variant B28Asp. *Biophysical Chemistry*. doi: 10.1016/j.bpc.2013.01.003

Renner, R., Pfützner, A., Trautmann, M., Harzer, O., Sauter, K., & Landgraf, R. (1999). Use of insulin lispro in continuous subcutaneous insulin infusion treatment: Results of a multicenter trial. *Diabetes Care*. doi: 10.2337/diacare.22.5.784

Simpson, K. L., & Spencer, C. M. (1999). Insulin aspart. *Drugs*, *57*(5), 759–765.

Sokalingam, S., Raghunathan, G., Soundrarajan, N., & Lee, S. G. (2012). A study on the effect of surface lysine to arginine mutagenesis on protein stability and structure using green fluorescent protein. *PLoS ONE*. doi: 10.1371/journal.pone.0040410

Sorkina, T., Cheng, M. H., Bagalkot, T. R., Wallace, C., Watkins, S. C., Bahar, I., & Sorkin, A. (2021). Direct coupling of oligomerization and oligomerization-driven endocytosis of the dopamine transporter to its conformational mechanics and activity. *Journal of Biological Chemistry*. doi: 10.1016/j.jbc.2021.100430

Stamati, A., Karagiannis, T., Tsapas, A., & Christoforidis, A. (2022). Efficacy and safety of ultra-rapid insulin analogues in insulin pumps in patients with Type 1 Diabetes Mellitus: A systematic review and meta-analysis. *Diabetes Research and Clinical Practice*. doi: 10.1016/j.diabres.2022.110144

Tandon, H., de Brevern, A. G., & Srinivasan, N. (2021). Transient association between proteins elicits alteration of dynamics at sites far away from interfaces. *Structure*. doi: 10.1016/j.str.2020.11.015

Tokumoto, S., Higo, N., & Sugibayashi, K. (2006). Effect of electroporation and pH on the iontophoretic transdermal delivery of human insulin. *International Journal of Pharmaceutics*. doi: 10.1016/j.ijpharm.2006.07.002

Warwicker, J., Charonis, S., & Curtis, R. A. (2014). Lysine and arginine content of proteins: Computational analysis suggests a new tool for solubility design. *Molecular Pharmaceutics*. doi: 10.1021/mp4004749

Wu, H., Zheng, W., Eram, M. S., Vhuiyan, M., Dong, A., Zeng, H., He, H., Brown, P., Frankel, A., Vedadi, M., Luo, M., & Min, J. (2016). Structural basis of arginine asymmetrical dimethylation by PRMT6. *Biochemical Journal*. doi: 10.1042/BCJ20160537

Xu, B., Jacobs, M. I., Kostko, O., & Ahmed, M. (2017). Guanidinium Group Remains Protonated in a Strongly Basic Arginine Solution. *ChemPhysChem*. doi: 10.1002/cphc.201700197

Zinman, B., Tildesley, H., Chiasson, J. L., Tsui, E., & Strack, T. (1997). Insulin lispro in CSII: Results of a double-blind crossover study. *Diabetes*. doi: 10.2337/diabetes.46.3.440